PAPER • OPEN ACCESS

Near-isotropic sub-Ångstrom 3d resolution phase contrast imaging achieved by end-to-end ptychographic electron tomography

To cite this article: Shengbo You *et al* 2025 *Phys. Scr.* **100** 015404

View the article online for updates and enhancements.

Physica Scripta

PAPER

Near-isotropic sub-Ångstrom 3d resolution phase contrast imaging achieved by end-to-end ptychographic electron tomography

Shengbo You [ID] , Andrey Romanov [ID] and Philipp M Pelz [ID]

Institute of Micro- and Nanostructure Research (IMN) & Center for Nanoanalysis and Electron Microscopy (CENEM), Friedrich Alexander-Universität Erlangen-Nürnberg, IZNF, 91058 Erlangen, Germany

E-mail: philipp.pelz@fau.de

Abstract

Three-dimensional atomic resolution imaging using transmission electron microscopes is a unique capability that requires challenging experiments. Linear electron tomography methods are limited by the missing wedge effect, requiring a high tilt range. Multislice ptychography can achieve deep sub-Ångstrom resolution in the transverse direction, but depth resolution is limited to 2 to 3 nanometers. In this paper, we propose and demonstrate an end-to-end approach to reconstructing the electrostatic potential volume of the sample directly from the 4D-STEM datasets. End-to-end multislice ptychographic tomography recovers several slices at each tomography tilt angle and compensates for the missing wedge effect. The algorithm is initially tested in simulation with a Pt@Al$_2$O$_3$ core–shell nanoparticle, where both heavy and light atoms are recovered in 3D from an unaligned 4D-STEM tilt series with a restricted tilt range of 90 degrees. We also demonstrate the algorithm experimentally, recovering a Te nanoparticle with sub-Ångstrom resolution.

Introduction

Transmission Electron Microscopy (TEM) is essential in imaging nano- and atomic-scale features in structural biology, chemistry, and material science. Advances in aberration correction [1] have enhanced TEM's capabilities, enabling it to image individual atoms and characterize structure defects in two-dimensional materials [2–4]. However, traditional TEM imaging techniques limit the sample thickness to a few nanometers to avoid non-linear effects such as multiple electron scattering. Multiple electron scattering in bulk materials results in unresolvable electron intensity distribution [5]. However, knowledge of the three-dimensional structure is critical in understanding the material's physical properties. Due to this, the study of imaging 3D structures has always been an essential area in electron microscopy.

One of materials science's most well-explored methods for imaging the 3D atomic structure is atomic resolution electron tomography (AET). By tilting the sample, AET records a series of 2D projections at multiple tilt angles and recovers the 3D structure of the material with atomic resolution [6–9]. The AET method collects the dataset using annular dark field (ADF) scanning transmission electron microscopy (STEM) and uses a linear forward model to reconstruct an atomic resolution volume. However, there are limitations with ADF-STEM datasets, including low contrast for light elements [10], requiring higher electron doses for beam-sensitive specimens [11]. Combining phase-contrast imaging with AET is an alternative method to overcome these limitations. Phase contrast imaging in TEM usually records images at different defocus or a single image with contrast transfer function correction. However, the phase contrast itself relies on the multiplicative assumption. Hence, non-linear effects, such as the unavoidable multiple scattering effect, can lead to the failure of the reconstruction. A solution to the inverse multiple scattering problem has been demonstrated at close to atomic resolution using phase contrast TEM combined with tilt- and defocus series measurements [12].

Ptychography is a computational phase contrast method that Hoppe initially proposed in the 1960s [13]. Modern implementations in the electron microscope often use a defocused probe to raster scan through the

specimen collecting a 4D dataset, with adjacent illuminated areas overlapped [14]. With the redundancies introduced from those overlapping areas, an iterative algorithm can recover the complex transfer function of both sample and illumination probe [15]. Without requiring prior knowledge of the sample, ptychography can reconstruct a thin material with resolution beyond the diffraction limit of the lenses [16]. The combination of ptychography and AET (PAET) has been proposed to image light atoms with 3D structure in simulation [10, 17]. With PAET, a series of 4D datasets is collected at each tilt angle followed by a ptychography reconstruction to generate a projected 2D complex image of the sample at each angle. Subsequently, the 3D structure of the sample is recovered using all the 2D images. PAET has been successfully demonstrated in an experiment solving a complex nanostructure in 3D with precise atomic location [18]. Low-dose ptychographic electron tomography has been used to image organic-inorganic hybrid nanostructures at nanometer resolution [19]. Compared to AET, PAET improves imaging contrast for weakly scattering atoms by utilizing a significant fraction of the scattered electrons [18].

Multislice ptychography (MSP) is another 3D imaging technique well known for solving the inverse multiple scattering problem. MSP considers thick materials a series of thin slices, each satisfying the multiplicative assumption. The electron beam sequentially interacts with each slice with near-field free space propagation in between. In the reconstruction, all slices of the specimen can be recovered separately. The combination of the multislice algorithm with ptychography was proposed in 2012 [20]. Together, they can reconstruct samples thicker than the depth of field without tilting the sample while increasing the spatial resolution [21]. Multislice electron ptychography was recently demonstrated most successfully [21] with lattice vibration-limited resolution and precise imaging of low Z atoms.

Previous simulation studies showed the promise of inverting the multi-slice propagation in electron microscopy [17, 22–24]. The forward models used in these studies did not include partial coherence effects or provide experimental demonstrations. Recent experimental work demonstrated the capability of inverse multi-slice algorithms to resolve weakly scattering clay materials [12] using plane-wave illumination but did not reach atomic resolution.

Our contribution beyond the state of the art is fourfold:

(1) We present an end-to-end reconstruction algorithm, from the 4D-STEM datasets to the electrostatic potential volume, for ptychographic tilt series datasets that incorporates all state-of-the-art developments of ptychographic reconstruction algorithms: a multi-slice forward model [20, 21], partial coherence modeling of the probe [25], position correction [26], and joint alignment of the tomographic parameters [18].

(2) We detail a practical initialization procedure and a reconstruction sequence for all nuisance parameters that allow the recovery of sub-Ångstrom resolution volumes from experimental 4D-STEM tilt-series data.

(3) We demonstrate this algorithm experimentally by imaging a Tellurium nanoparticle attached to a carbon nanotube with 0.82 Å full-period 3D resolution, determined by Fourier Shell Correlation. To our knowledge, this is the highest 3D resolution achieved in phase-contrast microscopy.

(4) By virtual subsampling, we demonstrate the dose-effectiveness of the algorithm on experimental data, allowing sub-Ångstrom resolution with 12x less fluence.

Method

Algorithm for experimental end-to-end reconstruction of ptychographic tilt-series

The reconstruction workflow consists of three steps, as shown in figures 1 (a)–(c). In the first step, a fast reconstruction using only the bright-field part of the 4D-STEM data is performed, which yields phase images and initial estimates for the first-order aberration coefficients. The goal of the second step, shown in figure 1(b), is to accurately estimate global tomographic alignment parameters, mixed state probes, and subpixel corrected scan positions for each tilt angle. For this purpose, we perform mixed-state single- or multi-slice ptychography reconstruction for each 4D-STEM dataset separately, depending on the sample thickness. We then form 2D phase projection images at each tilt angle by summation of all reconstructed slices, shown in the upper part of figure 1(b). These 2D phase projections form the input for a joint tomography and alignment procedure, which yields the global translation and rotation parameters and a medium-quality reconstructed volume.

Finally, the last step is to reconstruct the sample's 3D volume using the preprocessed 4D STEM datasets together with the initial mixed-state probes, sub-pixel probe positions, and global alignment parameters, as shown in figure 1(c).
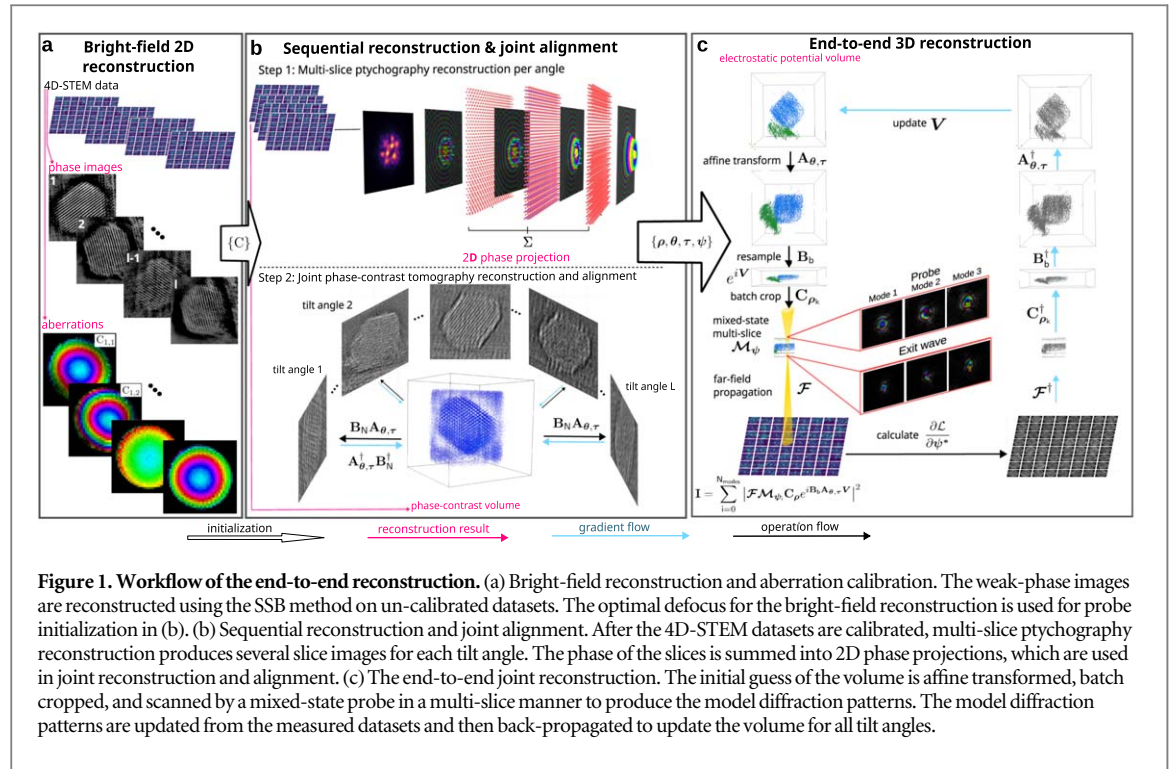
Figure 1. Workflow of the end-to-end reconstruction. (a) Bright-field reconstruction and aberration calibration. The weak-phase images are reconstructed using the SSB method on un-calibrated datasets. The optimal defocus for the bright-field reconstruction is used for probe initialization in (b). (b) Sequential reconstruction and joint alignment. After the 4D-STEM datasets are calibrated, multi-slice ptychography reconstruction produces several slice images for each tilt angle. The phase of the slices is summed into 2D phase projections, which are used in joint reconstruction and alignment. (c) The end-to-end joint reconstruction. The initial guess of the volume is affine transformed, batch cropped, and scanned by a mixed-state probe in a multi-slice manner to produce the model diffraction patterns. The model diffraction patterns are updated from the measured datasets and then back-propagated to update the volume for all tilt angles.

Bright-field reconstruction

In this work, we use a real-time implementation [27] of the single-sideband (SSB) [28] and weak-phase [29] ptychographic reconstruction algorithms to find an initial estimate of the first-order aberrations by maximizing the contrast in the reconstructed phase image, shown in figure 1(a). Another possible reconstruction method for this step is the parallax [30] or tilt-corrected bright-field STEM (tcBFSTEM) method [31]. Both methods work in focused and defocused conditions.

The SSB and weak-phase direct methods enjoy faster reconstruction due to lower computational complexity while requiring a Nyquist-sampled dataset. While the technique itself assumes a thin 2D object, its use has also been explored for thicker crystalline materials [32].

The tcBFSTEM method has a higher computational complexity but does not require a Nyquist-sampled dataset. This method has mainly been applied to biological specimens; the reliability of aberration recovery on thicker and crystalline specimens needs to be evaluated.

Therefore, the method of choice for this first aberration-estimation step depends on the experimental design and the size of the datasets.

Sequential Tomographic reconstruction and alignment

Multi-slice ptychography

This step aims to reconstruct a 2D projection for each tilt angle, which will be used in tomography to calculate the affine alignment in step 3. A single slice can be used to reconstruct samples that are not thicker than a few nanometers. However, the multiple scattering effects become significant for samples thicker than a few nanometers, and the multiplicative assumption is no longer valid. In this situation, our reconstruction pipeline uses multislice ptychography to solve this problem.

We review the equations leading to the multi-slice solution of multiple electron scattering to motivate our reconstruction algorithm [33]. The evolution of the slow-moving portion of the wavefunction along the optical axis z can be described by the Schrödinger equation for fast electrons [34]

$$\frac{\partial}{\partial z}\psi(\boldsymbol{r}) = \frac{i\lambda}{4\pi}\nabla_{xy}^{2}\ \psi(\boldsymbol{r}) + i\sigma V(\boldsymbol{r})\psi(\boldsymbol{r}), \tag{1}$$

where λ is the relativistic electron wavelength, ∇_{xy}^{2} is the 2D Laplacian operator, σ is the relativistic beam-sample interaction constant and $V(\boldsymbol{r})$ is the electrostatic potential of the sample. The formal operator solution to equation (1) is given by [34],

$$\psi_f(\boldsymbol{r}) = \exp\left\{\int_0^z \left[\frac{i\lambda}{4\pi}\nabla_{xy}^2 + i\sigma V(x, y, z')\right]dz'\right\}\psi_0(\boldsymbol{r}),\tag{2}$$

where $\psi_f(\boldsymbol{r})$ is the exit wavefunction after traveling a distance z from the initial wave $\psi_0(\boldsymbol{r})$. This expression is commonly approximately solved with the multislice algorithm first given by [5], which alternates solving the two operators using only the linear term in the series expansion of the exponential operator. In the multislice algorithm, we first divide up the sample of total thickness t into a series of thin slices with thickness Δz. Solving for the first operator on equation (2) yields an expression for free space propagation between slices separated by Δz, with the solution given by

$$\psi_f(\boldsymbol{r}) = \mathcal{P}^{\Delta z}\psi_0(\boldsymbol{r}),\tag{3}$$

where $\mathcal{P}^{\Delta z}$ is the Fresnel propagator defined by

$$\mathcal{P}^{\Delta z}\psi := \mathcal{F}_{\boldsymbol{q}}^{\dagger}[\mathcal{F}_{\boldsymbol{r}}[\psi]e^{-i\pi\lambda q^2 \Delta z}],\tag{4}$$

where $\boldsymbol{q} = (q_x, q_y)$ are the 2D Fourier coordinates and $\boldsymbol{r} = (x, y)$ are the 2D real space coordinates. $\mathcal{F}_{\boldsymbol{x}}[\,\cdot\,]$ denotes the two-dimensional Fourier transform with respect to $\boldsymbol{x}$ and $\mathcal{F}_{\boldsymbol{x}}^{\dagger}[\,\cdot\,]$ the 2D inverse Fourier transform with respect to $\boldsymbol{x}$. We can then write one iteration of the multislice algorithm as

$$\mathcal{T}^{V_k}\psi = \psi \cdot e^{i\sigma V_k}\tag{5}$$

where V_k is the potential at slice k.' We write multi-slice algorithm applied to a volume discretized into T slices $\mathcal{M}_\psi\colon \mathbb{C}^{N_1 \times N_2} \to \mathbb{C}^{N_1 \times N_2}$ as a succession of T pairs of transmission and propagation operators

$$\mathcal{M}_\psi(\boldsymbol{V}) = \prod_{k=0}^{\mathsf{T}} (\mathcal{P}^{\Delta z}\mathcal{T}^{V_k})\psi.\tag{6}$$

[33] The 4D-STEM intensity at probe position $\boldsymbol{\rho}_k$ is then

$$\boldsymbol{I}_k = |\mathcal{F}_{\boldsymbol{r}}[\mathcal{M}_{\psi(r-\rho_k)}(e^{i\sigma V})]|^2.\tag{7}$$

To decouple the sampling in the detector plane from the sampling in the specimen plane and to reduce the computational burden, we can introduce a linear batch-cropping operator $\mathbf{C_w} := \mathbb{C}^{N_1 \times N_2} \to \mathbb{C}^{W \times M_1 \times M_2}$, which extracts $W = \dim(\mathbf{w})$ real-space patches of size $M_1 \times M_2$ from each slice of the volume at the positions with indices $\mathbf{w}$. The multi-slice algorithm with batch-cropping is then

$$\mathcal{M}_\psi^{\mathbf{w}}(\boldsymbol{V}) = \prod_{k=0}^{\mathsf{T}} (\mathcal{P}^{\Delta z}\mathbf{C_w}\mathcal{T}^{V_k})\psi.\tag{8}$$

With this introduction, the 4D-STEM intensity of the diffraction patterns in batch $\mathbf{w}$ is then

$$\boldsymbol{I_w} = |\mathcal{F}_{\boldsymbol{r}}[\mathcal{M}_{\psi_i(r-\rho_{\mathbf{w}})}^{\mathbf{w}}(e^{i\sigma V})]|^2.\tag{9}$$

The remaining sub-pixel shift of the probe, which the cropping operation cannot achieve, is performed by multiplication with a phase-ramp in Fourier space. Up to this point, we assumed a perfectly coherent probe ψ. To model partial coherence, we, therefore, introduce a set of partially coherent modes $\{\boldsymbol{\psi}(\boldsymbol{r})_i\}_{i=0,\ldots,N_{modes}}$, and the measured intensity becomes the incoherent sum of these modes [25]

$$\boldsymbol{I_w} = \sum_{i=0}^{N_{modes}} |\mathcal{F}_{\boldsymbol{r}}[\mathcal{M}_{\psi_i(r-\rho_{\mathbf{w}})}^{\mathbf{w}}(e^{i\sigma V})]|^2,\tag{10}$$

which we use as the differentiable forward model in the MSP reconstruction algorithm 1. The edge cropping option is also available for large datasets to save computation time.

Algorithm 1. MultiSlicePtycho (MSP): Joint 3D object, mixed-state probe, and position retrieval using multi-slice ptychography

Input:		
	measured intensities	$\mathbf{I} \in \mathbb{R}^{K \times M_1 \times M_2}$
	scan positions	$\boldsymbol{\rho} \in \mathbb{R}^{K \times 2}$
	initial probe aberration	$C_1 \in \mathbb{R}$
	step sizes	$\gamma_1, \gamma_2 \in \mathbb{R}$
	position refinement start	$\mathrm{start}_\rho \in \mathbb{N}$
	probe refinement start	$\mathrm{start}_\psi \in \mathbb{N}$
	iteration number	$L \in \mathbb{N}$
	batch number	$\beta \in \mathbb{N}$

Initialize:

initialize aberration surface $\boldsymbol{\chi}^0$ from defocus C_1

calculate $\mathbf{I}^{mean} = \frac{1}{K}\sum_{k=1}^{K}\mathbf{I}_k$ and

$a_{max} = \max\{\|\mathbf{I}_k\|_1\ \forall\ k = \{1, ..., K\}\}$

set $\psi^0 \leftarrow \frac{a_{max}}{\sqrt{\|\mathbf{I}^{mean}\|_1}}\mathbf{I}^{mean}e^{i\chi^0}$

$V^0 \leftarrow \boldsymbol{0} \in \mathbb{C}^{N_0 \times N_1 \times N_2}$

divide diffraction patterns into β batches of adjacent scan indices $\boldsymbol{\Gamma}$

for l = 0 to L **do**

    reshuffle batch order $\boldsymbol{\Gamma}$

    for w in $\boldsymbol{\Gamma}$ **do**

        $\boldsymbol{I}_{\mathrm{model},\mathbf{w}} = \sum_{i=0}^{N_{modes}}|\mathcal{F}_r[\mathcal{M}_{\psi_i(r-\rho_\mathbf{k})}^{\mathbf{w}}(e^{i\sigma V})]|^2$

        $\mathcal{L}_\mathbf{w} = \|\sqrt{\mathbf{I}_{\mathrm{model},\mathbf{w}}} - \sqrt{\mathbf{I}_\mathbf{w}}\|^2$

        $V_\mathsf{n}^{l+1} = V_\mathsf{n}^l - \gamma_1\frac{\partial\mathcal{L}}{\partial V_\mathsf{n}}$ for all n $\in \{1...N_0\}$

        If l > start_ψ **then**

            $\psi_i^{l+1} = \psi_i^l - \gamma_2\frac{\partial\mathcal{L}}{\partial\psi_i}$ for all i

        If l > start_ρ **then**

            $\rho_\mathbf{w}^{l+1} = \rho_\mathbf{w}^l - \gamma_2\frac{\partial\mathcal{L}}{\partial\rho_\mathbf{w}}$ for all k

Output: $V^* = V^\mathsf{L}, \rho^* = \rho^\mathsf{L}, \psi^* = \psi^\mathsf{L}$

Joint rigid alignment and linear tomography

Since the electrostatic potential of the sample is reconstructed, a 2D projection of the sample V_{tot} can be formed by summing up the real part of all reconstructed slices.

$$V_{\mathrm{tot}} = \sum_{\mathsf{n}=0}^{N_0} \mathfrak{R}(V_n^*)$$

returns an $\mathbb{R}^{N_1 \times N_2}$ image for each angle. Using the potential projection for each angle from the multislice ptychography reconstruction, the affine transformation can be calculated using tomography, with the workflow shown in figure 1(b). The algorithm starts with loading the 2D projections and specifying the tilt angles. The 2D projections are preprocessed by applying an intensity threshold to flatten the background so that the outline of the nanoparticles is the most dominant feature in the image. Then, the images are down-sampled by averaging the adjacent pixels. Downsampling makes the algorithm focus on the outline of the particles, not misled by the smaller features inside them. These preprocessed images are considered as the sinogram target $\boldsymbol{y}_{\mathrm{measure\text{-}j}}$, at the j-th tilt angle of the loss function.

The affine alignment includes the 3D rotation angles $\boldsymbol{\Theta}$: $(\varphi, \psi, \theta) \in \mathbb{R}^{N_{\mathrm{angles}} \times 3}$ defined by Euler angles, more specifically the Tait-Bryan convention, and the 2D spatial translation $\boldsymbol{\tau} \in \mathbb{R}^{N_{\mathrm{angles}} \times 2}$. The rotation matrix $\mathbf{R}$ is defined following the tomography convention in the cryoEM processing package RELION [35]:

$$\mathbf{R}_{\Theta,\tau} = \mathbf{R}_\tau * \mathbf{R}_z * \mathbf{R}_y * \mathbf{R}_x, \tag{11}$$

with the second rotation around the Y-axis being the stage tilt axis, the third rotation around the Z-axis equationing the Y-axis in the projection image, and the first rotation accounting for non-perpendicularity of the stage axis to the optical axis. To keep all parameters differentiable, we implement the Radon transform with rotation and global translation with subsequent affine transformations and projection in Pytorch:

$$R_{\Theta,\tau} = \mathbf{A}_{0,\tau}\mathbf{B}_\mathbf{N}\mathbf{A}_{\Theta,0}, \tag{12}$$

where $\mathbf{B}_\mathbf{N}$ is a binning operator along the beam direction. The iterative tomography alignment process consists of two nested loops. The outer loop updates the alignment parameters, which are then fixed in the inner loop. The inner loop performs the tomography reconstruction using an adjoint Radon transform $R^\dagger_{\Theta,\tau}$ on a 3D model of the particle, with the 2D projection images and the alignment parameters from the outer loop. A new set of projection images at the same tilt angles of the 3D model of the particle is considered as the sinogram model.

$$\hat{\boldsymbol{y}} = R_{\Theta,\tau}V \tag{13}$$

The mean squared error loss function is calculated using the sinogram model $\hat{\boldsymbol{y}}$ and sinogram target $\boldsymbol{y}_{\mathrm{measure}}$, $\mathcal{L}_{MSE} = \|\hat{\boldsymbol{y}} - \boldsymbol{y}_{\mathrm{measure}}\|_2^2$.

The alignment parameters are then updated using gradient backpropagation using the autograd framework in pytorch to find optimal values. The spatial translation is fitted before the 3D rotation angles to save the computational burden. The algorithm is formally described in Algorithm 2. The recovered rotation angles and the spatial translation should be tuned to optimal values since these are not updated in the joint reconstruction. Inaccurately estimated values can lead to resolution and precision reduction. The quality of the alignment

parameters can be assessed by the reconstructed final aligned volume in Algorithm 2, one example is shown in figure 3(a).

Algorithm 2. JointLinearTomography : Joint volume, euler angle, and global translation reconstruction using SGD

Input:

	2D phase projections	$y_{\mathrm{measure}} \in \mathbb{R}^{N_{\mathrm{angles}} \times N_1 \times N_2}$
	initial euler angles	$\Theta^0 \in \mathbb{R}^{N_{\mathrm{angles}} \times 3}$
	initial global translations	$\tau^0 \in \mathbb{R}^{N_{\mathrm{angles}} \times 2}$
	step sizes	$\gamma_1, \gamma_2, \gamma_3 \in \mathbb{R}$
	iteration numbers	$\mathsf{T}, \mathsf{L} \in \mathbb{N}$

Initialize:

$V^0 \leftarrow \mathbf{0} \in \mathbb{R}^{N_0 \times N_1 \times N_2}$

joint alignment

for $\mathsf{l} = 0$ to L **do**

    $V^0 \leftarrow \mathbf{0}$

    for $\mathsf{t} = 0$ to T **do**

        $\hat{y} = R_{\Theta^{\mathsf{l}}, \tau^{\mathsf{l}}} V^{\mathsf{t}}$

        $\mathcal{L} = \| \hat{y} - y_{\mathrm{measure}} \|^2$

        $V^{\mathsf{t}+1} = V^{\mathsf{t}+1} - \gamma_1 \frac{\partial \mathcal{L}}{\partial V}$

    $\hat{y} = R_{\Theta^{\mathsf{l}}, \tau^{\mathsf{l}}} V^{\mathsf{T}}$

    $\mathcal{L}^{\mathsf{T}} = \| \hat{y} - y_{\mathrm{measure}} \|^2$

    $\tau^{\mathsf{l}+1} = \tau^{\mathsf{l}} - \gamma_2 \frac{\partial \mathcal{L}^{\mathsf{T}}}{\partial \tau_{\mathsf{l}}}$

    $\Theta^{\mathsf{l}+1} = \Theta^{\mathsf{l}} - \gamma_3 \frac{\partial \mathcal{L}^{\mathsf{T}}}{\partial \Theta_{\mathsf{l}}}$

reconstruct final aligned volume

for $\mathsf{t} = 0$ to T **do**

    $\hat{y} = R_{\Theta^{\mathsf{L}}, \tau^{\mathsf{L}}} V^{\mathsf{t}}$

    $\mathcal{L} = \| \hat{y} - y_{\mathrm{measure}} \|^2$

    $V^{\mathsf{t}+1} = V^{\mathsf{t}+1} - \gamma_1 \frac{\partial \mathcal{L}}{\partial V}$

Output: $V^* = V^{\mathsf{T}}, \Theta^* = \Theta^{\mathsf{L}}, \tau^* = \tau^{\mathsf{L}}$

End-to-end reconstruction

The end-to-end reconstruction uses 4D-STEM datasets from all tilt angles to directly recover the sample's electrostatic potential with isotropic sampling in 3D, together with mixed-state probes and subpixel positions. The volume of the 3D potential is initialized with zero - no prior knowledge of the sample is required. The initial guess of the probe is formed using the mixed-state probes reconstructed in step 1 of the sequential reconstruction, shown in figure 1(b). The initial parameters for the affine alignment, consisting of the 3D rotation angles and spatial translations, are also provided from Step 2 of the sequential reconstruction. The forward model of the end-to-end reconstruction is shown on the left side of figure 1(c). For every tilt angle, the reconstruction starts with rotating and translating the potential volume, denoted as V, using the determined affine alignment $A_{\Theta, \tau}: \mathbb{C}^{N_0 \times N_1 \times N_2} \to \mathbb{C}^{N_0 \times N_1 \times N_2}$. The transformed volume is then resampled along the beam propagation direction with the operator $\mathbf{B}_b: \mathbb{C}^{N_0 \times N_1 \times N_2} \to \mathbb{C}^{N_0/b \times N_1 \times N_2}$, with the slice number defined by the user. It is recommended to choose a slice thickness that slightly oversamples the depth of field of the probe. The resampled potential volume is then turned into a complex transfer function. The complex transfer function volume is cropped along the beam direction by the operator $\mathbf{C}_{\rho_l}: \mathbb{C}^{N_0/b \times N_1 \times N_2} \to \mathbb{C}^{N_0/b \times M_1 \times M_2}$ at each scan position ρ_l, into patches with sizes equal to the probe images. The exit wave of each slice is calculated using a batched multislice propagator $M_\psi^{\mathbf{w}}$, as described in step 1 of figure 1(b). The exit wave after the last slice is propagated to a detector placed in a far field and forms the model diffraction patterns, calculated using a 2D Fourier transform F. This is repeated for every coherent probe mode and the intensities are summed incoherently. With all operations in place, we define the end-to-end ptychographic tomography forward model $\mathcal{A}$ as

$$\mathcal{A}_{\psi, \rho, \Theta, \tau}(V) = \mathcal{F} M_{\psi_{l,i}}^{\mathbf{w}} (e^{i \mathbf{B}_b A_{\Theta_l} \tau_l V}) \tag{14}$$

and write it shorthand $\mathcal{A}(V)$. The model intensity with a low-rank mixed-state approximation is then

$$\mathbf{I}_m = \sum_{i=0}^{N_{\mathrm{modes}}} |\mathcal{A}_{\psi_i, \rho, \Theta, \tau}(V)|^2 \tag{15}$$

The loss function value is calculated using the amplitude of the modeled diffraction patterns and the measured 4D-STEM data. The gradients of the amplitude loss with respect to the volume and the wave function are

propagated back through the computational graph using the automatic gradient framework of the pytorch package [36].

$$\mathcal{L}_l^\epsilon = \| \sqrt{\mathbf{I_m} + \epsilon} - \sqrt{\mathbf{I_l} + \epsilon} \|_2^2 + \lambda \, \| \mathfrak{I}(\mathbf{V}) \|_1. \tag{16}$$

We employ L_1-regularization of the imaginary part of the potential, to suppress an overly large absorptive potential. The proximal operator of the L_1-norm is the well-known shrinkage operator

$$\text{shrink}(z, \mu\tau) = \text{sign}(z)\max(|z| - \mu\tau, 0), \tag{17}$$

which is applied after each minibatch.

As an example, we write out the gradients with respect to layer k of the volume:

$$\frac{\partial \mathcal{L}}{\partial \mathbf{V}_k^*} = \lim_{\epsilon \to 0} \frac{\partial \mathcal{L}_l^\epsilon}{\partial \mathbf{V}_k^*} = [i\sigma \mathbf{A}_{\Theta,\tau}^\dagger \mathbf{B}_b^\dagger [(\mathbf{C_w}\mathcal{T}^1)^\dagger \mathcal{P}^{-\Delta z}(\mathbf{C_w}\mathcal{T}^2)^\dagger \mathcal{P}^{-\Delta z} \ldots \tag{18}$$

$$\ldots (\mathbf{C_w}\mathcal{T}^N)^\dagger (\mathcal{F}^\dagger (\mathcal{A}(\mathbf{V}) - \sqrt{\mathbf{I}} * \text{sgn}(\mathcal{A}(\mathbf{V}))))]]_k. \tag{19}$$

Then, the reconstruction proceeds to the next tilt angle, and the current volume is the updated one from the previous tilt angle. In other words, the initial guess of the volume for the next angle is the updated volume from the previous angle. The reconstruction updates the same volume for all the tilt angles, typically requiring a few hundred iterations until convergence. We also experimented with gradient accumulation over multiple angles before a gradient step. However, this results in slower convergence and was therefore not analyzed in detail. The faster convergence of minibatch or stochastic gradient methods is known from other ptychographic algorithms [37]. The joint reconstruction is formalized in Algorithm 3.

Algorithm 3. End2EndPtychoTomo: Joint volume, position, and multi-modal probe retrieval via minibatch SGD

Input:

measured intensities	$\mathbf{I} \in \mathbb{R}^{N_{angles} \times K \times M_1 \times M_2}$	
scan positions	$\rho \in \mathbb{R}^{N_{angles} \times K \times 2}$	
euler angles	$\Theta \in \mathbb{R}^{N_{angles} \times 3}$	
global translations	$\tau \in \mathbb{R}^{N_{angles} \times 2}$	
initial probe modes	$\psi \in \mathbb{C}^{N_{angles} \times N_m \times M_x \times M_y}$	
step sizes	$\gamma_1, \gamma_2, \gamma_3 \in \mathbb{R}$	
binning	$b \in \mathbb{N}$	
iteration number	$E \in \mathbb{N}$	

Initialize:

$\mathbf{V}^0 \leftarrow \mathbf{0} \in \mathbb{C}^{N_0 \times N_1 \times N_2}$

divide diffraction patterns into β batches of adjacent scan indices Γ

for $e = 0$ to E **do**
    for $l = 0$ to N_{angles} **do**
        reshuffle batch order Γ
        for w in Γ **do**
            $\mathbf{I}_m = \sum_{i=0}^{N_{modes}} |\mathcal{A}_{\psi_{l,w}, \rho, \Theta, \tau}(\mathbf{V})|^2$
            $\mathcal{L} = \| \sqrt{\mathbf{I}_m} - \sqrt{\mathbf{I}_{l,w}} \|^2$
            $\mathbf{V}^{l+1} = \mathbf{V}^l - \gamma_1 \frac{\partial \mathcal{L}}{\partial \mathbf{V}^{l,*}}$
            if $l > \text{start}_\psi$ **then**
                $\psi_{l,w}^{l+1} = \psi^l - \gamma_2 \frac{\partial \mathcal{L}}{\partial \psi_{l,w}^*}$
            if $l > \text{start}_\rho$ **then**
                $\rho_{l,w}^{l+1} = \rho_{l,w}^l - \gamma_3 \frac{\partial \mathcal{L}}{\partial \rho_{l,w}}$
            $\text{shrink}(\mathfrak{I}(\mathbf{V}), \lambda)$
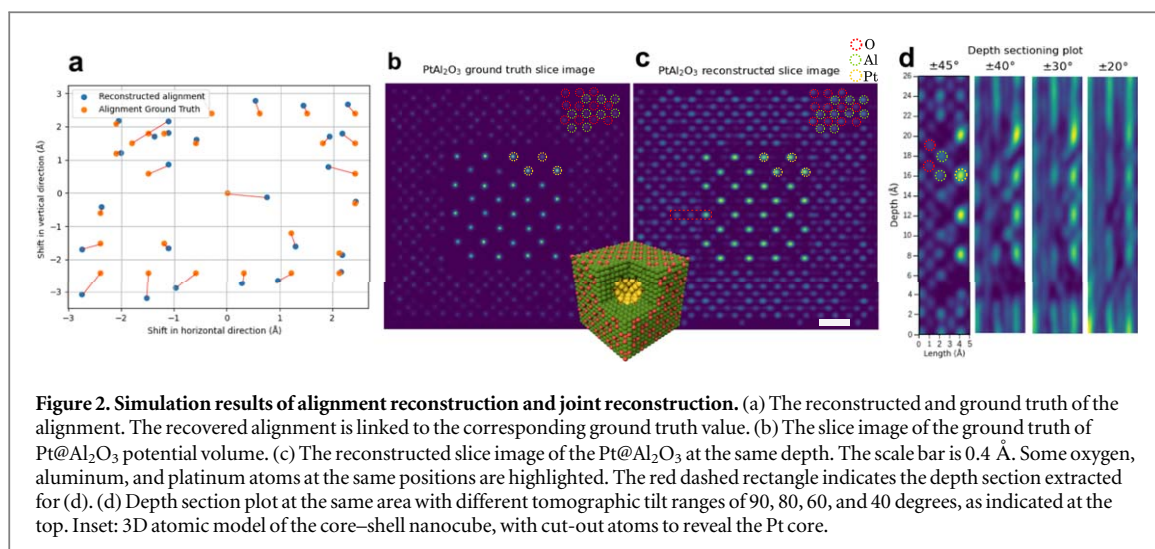 $\mathbf{V}^0 \leftarrow \mathbf{V}^{N_{angles}}$
$\mathbf{V}^E \leftarrow \mathbf{V}^0$
Output: $\mathbf{V}^* = \mathbf{V}^E$

Results

Alignment precision and reconstruction quality using simulated data

A simulation benchmark was built to test the algorithm's performance. A cube-shaped Pt@Al_2O_3 core-shell nanoparticle was constructed to evaluate the precision of the recovery of alignment parameters and the ability to image low-Z atoms alternating with heavier atoms along the beam propagation direction at 0∘ tilt. The electrostatic potential volume of the sample was built using the Prismatic 2.0 [38] simulation code using ten

Figure 2. Simulation results of alignment reconstruction and joint reconstruction. (a) The reconstructed and ground truth of the alignment. The recovered alignment is linked to the corresponding ground truth value. (b) The slice image of the ground truth of Pt@Al$_2$O$_3$ potential volume. (c) The reconstructed slice image of the Pt@Al$_2$O$_3$ at the same depth. The scale bar is 0.4 Å. Some oxygen, aluminum, and platinum atoms at the same positions are highlighted. The red dashed rectangle indicates the depth section extracted for (d). (d) Depth section plot at the same area with different tomographic tilt ranges of 90, 80, 60, and 40 degrees, as indicated at the top. Inset: 3D atomic model of the core–shell nanocube, with cut-out atoms to reveal the Pt core.

frozen phonons. Ten frozen phonon 4D-STEM datasets were collected and then averaged. The same procedure was repeated for all tilt angles. To test the performance of the alignment algorithm, relative shifts with a maximum of 3.4 Å among the tilt angle datasets are sampled uniformly for each tilt angle and recorded as ground truth global translations τ_{gt}. An MSP reconstruction is performed for each tilt angle, producing a 10-slice volume, which is then summed up to a 2D phase projection for each tilt angle. The 2D phase projections were fed into the JointLinearTomo algorithm, producing an initial volume V and the global alignment parameters Θ^* and τ^*. The reconstructed alignment and the alignment ground truth were plotted in figure 2(a). Compared to the ground truth, half of the reconstructed alignment had differences within 0.4 Å, with the maximum difference being 0.8 Å. Such an alignment error is acceptable, given the Nyquist resolution in our experiments was 0.8 Å. A subsequent position optimization in the end-to-end algorithm can be performed to improve further the alignment to achieve deep sub-Ångstrom 3D resolution.

The volume result from the joint reconstruction showed high accuracy. With the slice images at the same depth (both with a thickness of 1 Å) shown in figures 2(b)–(c). Both high-Z atoms, platinum, and low-Z atoms, as well as oxygen, were recovered and present in the slice images. Some 'shadow' or 'faded atoms' appeared in the middle area of the reconstructed slice image. This was mainly due to the cross-talk between slices. The atoms located in the adjacent slices were not perfectly decoupled. This was reasonable considering the electron dose for each tilt angle was chosen as $1.9 \times 10^4\ e/\text{Å}^2$, with 27 angles within the range of $\pm 45\circ$, $5.13 \times 10^5\ e/\text{Å}^2$ for the entire tilt series.

Another test was to determine the minimum tilt range to separate atoms in the depth direction under low-dose conditions clearly. The dose for a single tilt angle and the tilt angle increment step were kept the same, but the tilt ranges differed, as shown in figure 2(d). The platinum atoms can be separated within $\pm 20\circ$. Oxygen and aluminum atoms were recovered with reasonable resolution at $\pm 45\circ$.

Experimental demonstration

The experimental setup for the demonstration of the end-to-end reconstruction is identical to the experimental setup for PAET [18]. A converged electron probe with a semi-convergence angle of 25 mrad is raster scanned over a Te particle sitting on a carbon nanotube with 800x800 positions and a diffraction pattern recorded at each scan position, forming a 4D-STEM dataset. The sample preparation is described in Supplementary section 1. The 220x220 scan positions that cover the particle were used for reconstruction. The experimental parameters are given in Supplementary table 1 and the data acquisition is described in Supplementary Materials section 2. A mixed-state probe with three coherent modes was used for partial coherence modeling [25], with three example modes shown in figure 1(c). The nanoparticle was then tilted around its axis, and the same 4D-STEM collection procedure was performed at each tilt angle. 26 angles were collected in a tilt series ranging from -53 to 52 degree. With 220 scan points in both x and y directions, diffraction patterns being 66 pixels, and a 5-pixel margin at the edge of the scan positions, a $296 \times 296 \times 296$-pixel volume, corresponding to a $(11.8\ \text{nm})^3$, was used as an initial guess of the sample's potential. During the reconstruction of each angle, the datasets were divided into five batches and loaded onto the GPU. Together with the volume to be reconstructed and other data, such as probe and scan positions, it required 24GB GPU usage. Assuming the volume contained eight slices, each with a thickness of 1.475 nm, it took no more than 4 seconds per iteration for each tilt angle. With 26 tilt angles and 300 iterations, the total reconstruction time was roughly 8 hours.
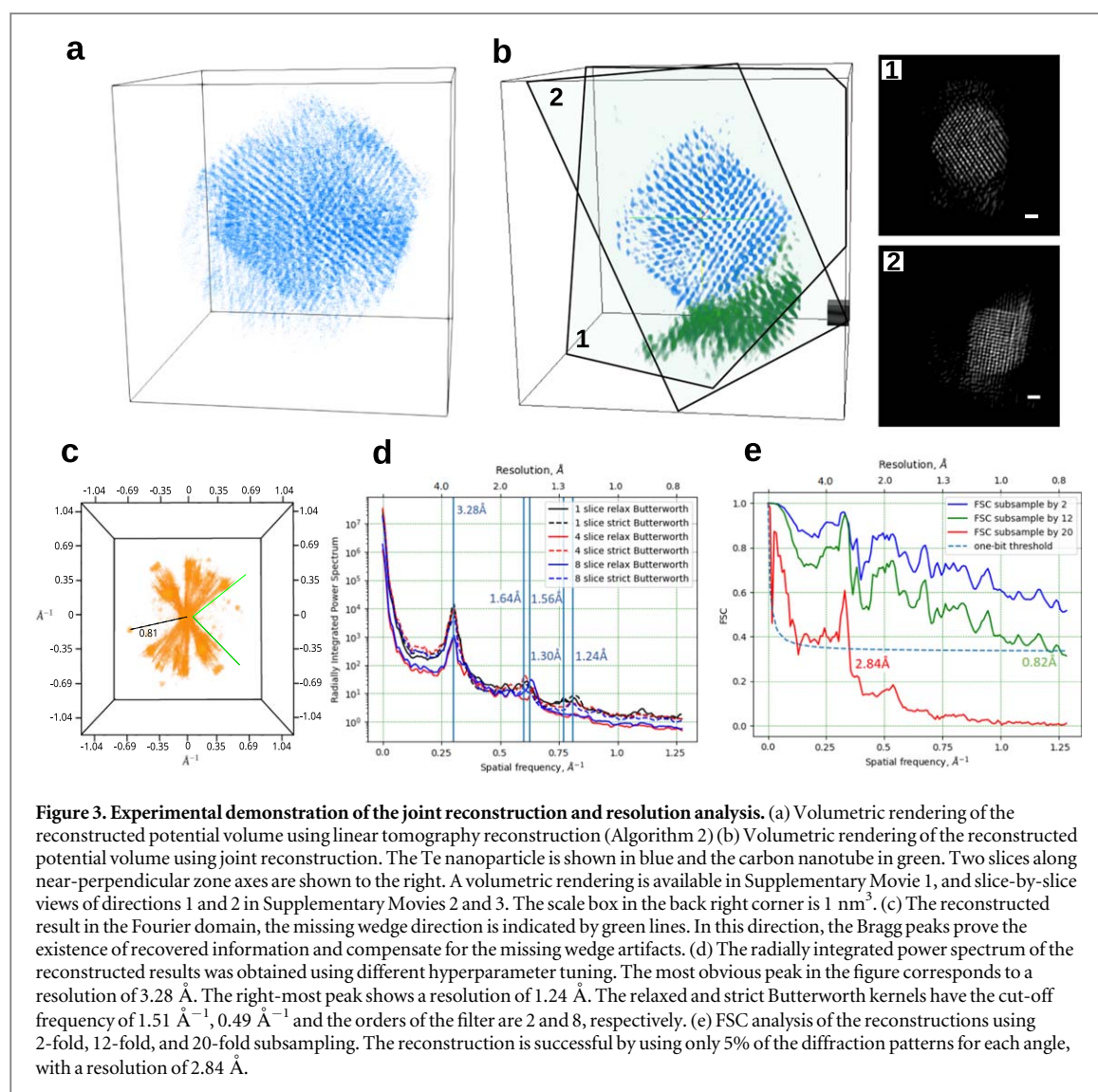
Figure 3. Experimental demonstration of the joint reconstruction and resolution analysis. (a) Volumetric rendering of the reconstructed potential volume using linear tomography reconstruction (Algorithm 2) (b) Volumetric rendering of the reconstructed potential volume using joint reconstruction. The Te nanoparticle is shown in blue and the carbon nanotube in green. Two slices along near-perpendicular zone axes are shown to the right. A volumetric rendering is available in Supplementary Movie 1, and slice-by-slice views of directions 1 and 2 in Supplementary Movies 2 and 3. The scale box in the back right corner is 1 nm^3. (c) The reconstructed result in the Fourier domain, the missing wedge direction is indicated by green lines. In this direction, the Bragg peaks prove the existence of recovered information and compensate for the missing wedge artifacts. (d) The radially integrated power spectrum of the reconstructed results was obtained using different hyperparameter tuning. The most obvious peak in the figure corresponds to a resolution of 3.28 Å. The right-most peak shows a resolution of 1.24 Å. The relaxed and strict Butterworth kernels have the cut-off frequency of 1.51 Å^{-1}, 0.49 Å^{-1} and the orders of the filter are 2 and 8, respectively. (e) FSC analysis of the reconstructions using 2-fold, 12-fold, and 20-fold subsampling. The reconstruction is successful by using only 5% of the diffraction patterns for each angle, with a resolution of 2.84 Å.

Ablation study

Similar to the simulation, the multislice ptychography and alignment procedure were performed before the joint reconstruction. A Butterworth kernel was used to filter out the high-frequency noise with a cut-off frequency of 1.51 Å^{-1} and the order of the filter being 2. L1 regularization was applied to the real part of the potential after the first 150 iterations of the joint reconstruction. We also applied a nonnegativity constraint to eliminate the meaningless negative part of the reconstructed potential, with a penalty number of 1×10^{-7} per iteration. A regularization kernel [39] was used to ensure a uniform intensity distribution between slices of the volume. In our case, the regularization kernel is in the shape of $5 \times 5 \times 73$ pixels with a regularization parameter of 90. A larger regularization parameter will force a lower resolution in the propagation direction of the currently reconstructed angle. However, it will make the regularization kernel larger in space, occupying more GPU memory and computational resources. Hence, the regularization parameter is chosen at a compromise with intensity distribution at an acceptable level, and the additional computation burden is reasonable. We performed a small ablation study on the influence of the different hyperparameters. The performance of the joint reconstruction was tested using different parameter combinations of the above kernels and different numbers of slices. The other reconstruction parameters were kept the same for the test, such as 300 iterations for the reconstruction and a step size of 1.

Radially integrated power spectrum analysis was used to analyze the effect of the hyperparameters. Some results are shown in figure 3(d). The relaxed and strict Butterworth kernels had the cut-off frequency of 1.51 Å^{-1}, 0.49 Å^{-1} and the orders of the filter were 2, and 8 respectively. The entire sample volume had a thickness of 11.8 nm. Hence, the 1, 4, and 8 slices corresponded to a slice thickness of 11.8 nm, 2.95 nm, and 1.475 nm, respectively.

The first peak occurred at the 3.28 Å. At the high-resolution part of the spectrum, a more strict Butterworth filter with a cut-off frequency of 0.49 Å^{-1} and the order of the filter being 8 erases more noise, returning a slightly better resolution and a more obvious peak.

3D Sub-sampling and low-dose performance

To experimentally demonstrate the advantages of joint reconstruction under low dose conditions, we virtually reduced the total fluence by skipping several diffraction patterns in each dataset for the entire tilt series and performing two reconstructions of independent subsets of the 4D-STEM data. This is motivated by the observation that alternative scanning schemes can reduce beam damage when imaging radiation-sensitive materials [40, 41] and the ability of ptychography to reconstruct high-quality images and volumes with subsampled data. We compute the Fourier Shell Correlation (FSC) [42] of these independent reconstructions to obtain a resolution estimate, shown in figure 3(e) for three different amounts of subsampling. With the minimum required subsampling, a dataset division into two independent parts, the FSC reaches the Nyquist resolution of 0.8 Å without intersecting with the one-bit threshold. This indicates that we could further increase the resolution of the reconstruction by virtually extending the maximum detector angle and reconstructing a volume with smaller real-space sampling. This will be part of future studies as we increase the efficiency and runtime of our implementation. With independent datasets using 1/12th of the diffraction patterns, the one-bit threshold criterion intersects with the FSC curve at 0.82 Å. This means that sub-Å 3D resolution is possible for our Te metallic nanoparticle with a total fluence of $5.23 \times 10^4 \, e/\text{Å}^2$, combining a 12x fluence reduction with a resolution improvement compared to the previous PAET result [18] with a sequential reconstruction and identical experimental parameters. Reducing the subsampling further to 1/20th of the fully sampled dataset, our end-to-end reconstruction algorithm is still able to recover the volume with a resolution of 2.84 Å shown in the red FSC curve in figure 3(e). This amount of subsampling corresponds to a total fluence of $2.21 \times 10^4 \, e/\text{Å}^2$ for the whole tilt series, which shows the potential of end-to-end ptychographic tomography for use in imaging beam-sensitive materials.

Recovery of traditionally missing information
One common limitation in electron tomography is a restricted tilt range due to the strong electron-matter interaction and the resulting limitation on sample thickness. This limitation can only be avoided entirely with specialized needle geometries [43, 44]. For traditional linear electron tomography, the restricted tilt range results in unmeasured information in the corresponding directions, and the reconstructed volume suffers from artifacts such as elongation and streaking. Popular methods of compensating for this effect involve the implementation of a dual-axis sample holder [45, 46], which reduces the missing wedge of a single-tilt experiment to a missing pyramid by tilting the sample in two different axes, or conical tomography [47] resulting in a missing cone of information. Algorithmic methods to reduce missing wedge artifacts typically utilize prior information about the sample, such as piecewise smoothness [48], a limited number of material compositions [49], or representability by a low-dimensional dictionary [50]. End-to-end multislice ptychographic tomography provides a new method to compensate for the missing wedge effect by heavily utilizing physical priors. The multi-slice algorithm expands the 2D projection to a 3D volume at each tilt angle. In Fourier space, the information transfer of the joint reconstruction covers a larger area than the conventional tomography and is not limited to a thin slice. As a result, additional information is recovered in the missing wedge direction, indicated by the Bragg peaks in the Fourier space in figure 3(c). In real space, even with a 90 degree missing wedge, the reconstructed atoms in the beam sectioning direction are only slightly elongated, and the streaking effect is much less severe, as shown in figure 2(d).

Discussion

Our algorithm shows great potential under low-dose conditions. One possible future trend would be to apply this method to biological samples where the experimental conditions are stricter [51]. With the recent demonstration of sub-nm resolution in single-particle cryo-electron ptychography [52] and recent developments in the automation of cryo-4D-STEM experiments [53], this application of end-to-end multi-slice ptychographic tomography is right around the corner. A near-isotropic 3D resolution was achieved with a tilt range of $\pm 45°$ in the simulation and $\pm 53°$ in the experiment, with relatively low electron doses compared to previous experimental dose usage.

Conclusion

We introduce an end-to-end joint reconstruction algorithm with a practical initialization procedure that recovers a 3D volume of the sample directly from unaligned 4D-STEM measurements. In simulation, we have demonstrated the ability to image both high- and low-Z atoms in the same volume with a tilt range of only 90 degrees. We also experimentally demonstrated the algorithm on volume containing a Te nanoparticle and a carbon nanotube. By artificially subsampling the data, we have performed a low-dose reconstruction, yielding sub-Ångstrom resolution with 12x less dose than previously used, and 2.84 Å resolution with 20x less dose and a total fluence of $2.21 \times 10^4 \, e/\text{Å}^2$. The end-to-end algorithm also provides a method to compensate for the missing wedge effect of linear tomography experiments without any additional hardware requirement, as shown in both simulation and experiment. To further improve the resolution to the deep sub-Ångstrom regime, we expect performing sub-pixel position refinement in the end-to-end reconstruction will be necessary. In this article, we focus solely on the resolution of the reconstructed volumes. As atomic structure determination is usually the goal of atomic resolution imaging, a common subsequent step is atom tracing or atomic model building using the reconstructed volume. After this step, the precision and accuracy of the determined atomic coordinates are usually the quantities of interest. We leave this step as future work, as we believe this task is also best solved in an end-to-end fashion, as indicated by some recent works achieving end-to-end reconstruction for crystalline samples from a single 4D-STEM dataset [54, 55]. Another interesting future work would be to increase the electron doses while reducing the tilt range and determining the threshold for 3D sub-Ångstrom resolution. This acquisition scheme is interesting for radiation-resistant samples because decreasing the number of necessary tilts reduces the data acquisition time. As seen in previous simulation work [17, 22, 23], the depth resolution of inverse multi-slice algorithms depends on the sample scattering power, incident energy, and sample thickness, so there are many application-tailored experimental configurations to explore in the future.

Acknowledgments

Conflict-of-interest statement

The authors have no conflicts of interest to declare.

Data availability statement

The data supporting this study's findings are openly available at the following URL/DOI: https://doi.org/10.5281/zenodo.13060513.

Author contributions

S.Y. performed the ptychographic tomography reconstructions, and S.Y., A.R., and P.M.P. implemented the reconstruction algorithms. P.M.P. designed and performed the 4D-STEM tomography experiments, and P.M.P. conceived the study. S.Y. and P.M.P. wrote the manuscript.

Code availability

The code supporting the article is published on Github at the following URL: https://github.com/ECLIPSE-Lab/End2EndPtychoTomo_code

ORCID iDs

Shengbo You ⓘ https://orcid.org/0009-0008-0739-9903
Andrey Romanov ⓘ https://orcid.org/0000-0001-6342-6568
Philipp M Pelz ⓘ https://orcid.org/0000-0002-8009-4515

References

[1] Haider M, Uhlemann S, Schwan E, Rose H, Kabius B and Urban K 1998 Electron microscopy image enhanced *Nature* **392** 768–9
[2] Meyer J C, Girit C O, Crommie M F and Zettl A 2008 Imaging and dynamics of light atoms and molecules on graphene *Nature* **454** 319–22
[3] Krivanek O L *et al* 2010 Atom-by-atom structural and chemical analysis by annular dark-field electron microscopy *Nature* **464** 571–4
[4] Huang P Y *et al* 2011 Grains and grain boundaries in single-layer graphene atomic patchwork quilts *Nature* **469** 389–92
[5] Cowley J M and Moodie A F 1957 The scattering of electrons by atoms and crystals. i. a new theoretical approach *Acta Crystallographica* **10** 609–19
[6] Chen C-C, Zhu C, White E R, Chiu C-Y, Scott M C, Regan B C, Marks L D, Huang Y and Miao J 2013 Three-dimensional imaging of dislocations in a nanoparticle at atomic resolution *Nature* **496** 74–7
[7] Zhou J *et al* 2019 Observing crystal nucleation in four dimensions using atomic electron tomography *Nature* **570** 500–3
[8] Xu R *et al* 2015 Three-dimensional coordinates of individual atoms in materials revealed by electron tomography *Nature Materials* **14** 1099–103
[9] Yang Y *et al* 2017 Deciphering chemical order/disorder and material properties at the single-atom level *Nature* **542** 75–9
[10] Chang D J, Kim D S, Rana A, Tian X, Zhou J, Ercius P and Miao J 2020 Ptychographic atomic electron tomography: Towards three-dimensional imaging of individual light atoms in materials *Physical Review* B **102** 174101
[11] Ophus C, Ciston J, Pierce J, Harvey T R, Chess J, McMorran B J, Czarnik C, Rose H H and Ercius P 2016 Efficient linear phase contrast in scanning transmission electron microscopy with matched illumination and detector interferometry *Nature Communications* **7** 10719
[12] Whittaker M L, Ren D, Ophus C, Zhang Y, Waller L, Gilbert B and Banfield J F 2022 Ion complexation waves emerge at the curved interfaces of layered minerals *Nature Communications* **13** 3382
[13] Hoppe W 1969 Beugung im inhomogenen primärstrahlwellenfeld. i. prinzip einer phasenmessung von elektronenbeugungsinterferenzen *Acta Crystallographica Section A: Crystal Physics, Diffraction, Theoretical and General Crystallography* **25** 495–501
[14] Rodenburg J M and Faulkner H M L 2004 A phase retrieval algorithm for shifting illumination *Applied Physics Letters* **85** 4795–7
[15] Maiden A M and Rodenburg J M 2009 An improved ptychographical phase retrieval algorithm for diffractive imaging *Ultramicroscopy* **109** 1256–62
[16] Jiang Y *et al* 2018 Electron ptychography of 2d materials to deep sub-Ångström resolution *Nature* **559** 343–9
[17] Van den Broek W and Koch C T 2012 Method for retrieval of the three-dimensional object potential by inversion of dynamical electron scattering *Phys. Rev. Lett.* **109** 245502
[18] Pelz P M, Griffin S M, Stonemeyer S, Popple D, DeVyldere H, Ercius P, Zettl A, Scott M C and Ophus C 2023 Solving complex nanostructures with ptychographic atomic electron tomography *Nature Communications* **14** 7906
[19] Ding Z *et al* 2022 Three-dimensional electron ptychography of organic-inorganic hybrid nanostructures *Nature Communications* **13** 4787
[20] Maiden A M, Humphry M J and Rodenburg J M 2012 Ptychographic transmission microscopy in three dimensions using a multi-slice approach *JOSA* A **29** 1606–14
[21] Chen Z, Jiang Y, Shao Y-T, Holtz M E, Odstrčil M, Guizar-Sicairos M, Hanke I, Ganschow S, Schlom D G and Muller D A 2021 Electron ptychography achieves atomic-resolution limits set by lattice vibrations *Science* **372** 826–31
[22] Van den Broek W and Koch C T 2013 General framework for quantitative three-dimensional reconstruction from arbitrary detection geometries in tem *Phys. Rev.* B **87** 184108
[23] Lee J, Lee M, Park Y K, Ophus C and Yang Y 2023 Multislice electron tomography using four-dimensional scanning transmission electron microscopy *Physical Review Applied* **19** 054062
[24] Ren D, Ophus C, Chen M and Waller L 2020 A multiple scattering algorithm for three dimensional phase contrast atomic electron tomography *Ultramicroscopy* **208** 112860
[25] Thibault P and Menzel A 2013 Reconstructing state mixtures from diffraction measurements *Nature* **494** 68–71
[26] Maiden A M, Humphry M J, Sarahan M C, Kraus B and Rodenburg J M 2012 An annealing algorithm to correct positioning errors in ptychography *Ultramicroscopy* **120** 6472
[27] Pelz P M, Johnson I, Ophus C, Ercius P and Scott M C 2022 Real-time interactive 4d-stem phase-contrast imaging from electron event representation data: Less computation with the right representation *IEEE Signal Processing Magazine* **39** 2531
[28] Pennycook T J *et al* 2015 Efficient phase contrast imaging in stem using a pixelated detector. part 1: Experimental demonstration at atomic resolution *Ultramicroscopy* **151** 160–7
[29] Yang H, Ercius P, Nellist P D and Ophus C 2016 Enhanced phase contrast transfer using ptychography combined with a pre-specimen phase plate in a scanning transmission electron microscope *Ultramicroscopy* **171** 117125
[30] Varnavides G, Ribet S M, Zeltmann S E, Yu Y, Savitzky B H, Byrne D O, Allen F I, Dravid V P, Scott M C and Ophus C 2024 *Iterative Phase Retrieval Algorithms for Scanning Transmission Electron Microscopy* arXiv:2309.05250
[31] Yu Y *et al* 2024 Dose-efficient cryo-electron microscopy for thick samples using tilt-corrected scanning transmission electron microscopy, demonstrated on cells and single particles page 2024.04.22.590491
[32] Gao C, Hofer C, Jannis D, Bch A, Verbeeck J and Pennycook T J 2022 Overcoming contrast reversals in focused probe ptychography of thick materials: An optimal pipeline for efficiently determining local atomic structure in materials science *Applied Physics Letters* **121** 081906
[33] Pelz P M, Rakowski A, DaCosta L R, Savitzky B H, Scott M C and Ophus C 2021 A fast algorithm for scanning transmission electron microscopy imaging and 4d-stem diffraction simulations *Microscopy and Microanalysis* **27** 835–48
[34] Kirkland E J 2020 *Advanced Computing in Electron Microscopy 3rd Edition* (Springer)

[35] Burt A, Toader B, Warshamanage R, Kgelgen A, Pyle E, Zivanov J, Kimanius D, Bharat T A M and Scheres S H W 2024 *FEBS Open Bio* **14** 1788

[36] Paszke A *et al* 2019 Pytorch: an imperative style, high-performance deep learning library *Advances in Neural Information Processing Systems* **32**

[37] Tripathi A, Wendy Di Z, Jiang Z and Wild S M 2024 Stochastic minibatch approach to the ptychographic iterative engine *Optics Express* **32** 30199–225

[38] Rangel DaCosta L *et al* 2021 Prismatic 2.0-simulation software for scanning and high resolution transmission electron microscopy (stem and hrtem) *Micron* **151** 103141

[39] Chen Z *et al* 2021 Electron ptychography achieves atomic-resolution limits set by lattice vibrations *Science* **372** 826–31

[40] Velazco A, Bch A, Jannis D and Verbeeck J 2022 Reducing electron beam damage through alternative stem scanning strategies, part i: Experimental findings *Ultramicroscopy* **232** 113398

[41] Jannis D, Velazco A, Bch A and Verbeeck J 2022 Reducing electron beam damage through alternative stem scanning strategies, part ii: Attempt towards an empirical model describing the damage process *Ultramicroscopy* **240** 113568

[42] Van Heel M and Schatz M 2005 Fourier shell correlation threshold criteria q *J. Struct. Biol.* **151** 250262

[43] Barnard D P, Turner J N, Frank J and McEwen B F 1992 A 360 single-axis tilt stage for the high-voltage electron microscope *Journal of Microscopy* **167** 39–48

[44] Padgett E, Hovden R, DaSilva J C, Levin B D A, Grazul J L, Hanrath T and Muller D A 2017 A simple preparation method for full-range electron tomography of nanoparticles and fine powders *Microscopy and Microanalysis* **23** 11501158

[45] Mastronarde D N 1997 Dual-axis tomography: an approach with alignment methods that preserve resolution *Journal of Structural Biology* **120** 343–52

[46] Arslan I, Tong J R and Midgley P A 2006 Reducing the missing wedge: High-resolution dual axis tomography of inorganic materials *Ultramicroscopy* **106** 994–1000

[47] Lanzavecchia S, Cantele F, Bellon P L, Zampighi L, Kreman M, Wright E and Zampighi G A 2005 Conical tomography of freeze-fracture replicas: a method for the study of integral membrane proteins inserted in phospholipid bilayers *Journal of Structural Biology* **149** 87–98

[48] Goris B, Van den Broek W, Batenburg K J, Heidari Mezerji H and Bals S 2012 Electron tomography based on a total variation minimization reconstruction technique *Ultramicroscopy* **113** 120–30

[49] Zhuge X, Jinnai H, Dunin-Borkowski R E, Migunov V, Bals S, Cool P, Bons A-J and Batenburg K J 2017 Automated discrete electron tomography towards routine high-fidelity reconstruction of nanomaterials *Ultramicroscopy* **175** 8796

[50] Arenas Esteban D, Wang D, Kadu A, Olluyn N, Snchez-Iglesias A, Gomez-Perez A, Gonzlez-Casablanca J, Nicolopoulos S, Liz-Marzn L M and Bals S 2024 Quantitative 3d structural analysis of small colloidal assemblies under native conditions by liquid-cell fast electron tomography *Nature Communications* **15** 6399

[51] Pei X *et al* 2023 Cryogenic electron ptychographic single particle analysis with wide bandwidth information transfer *Nature Communications* **14** 3027

[52] Kkoglu B *et al* 2024 Low-dose cryo-electron ptychography of proteins at sub-nanometer resolution *Nat Commun* **15** 8062

[53] Seifer S, Kirchweger P, Edel K M and Elbaum M 2024 Optimizing contrast in automated 4d stem cryotomography *Microscopy and Microanalysis* **30** 476488

[54] Diederichs B, Herdegen Z, Strauch A, Filbir F and Mller-Caspary K 2024 Exact inversion of partially coherent dynamical electron scattering for picometric structure retrieval *Nature Communications* **15** 101

[55] Yang W, Sha H, Cui J, Mao L and Yu R 2024 Local-orbital ptychography for ultrahigh-resolution imaging *Nature Nanotechnology* **16**